TWO-DIMENSIONAL TOMOGRAPHIC INVERSION WITH FINITE-DIFFERENCE TRAVELTIMES

DAVID F. ALDRIDGE [1] and DOUGLAS W. OLDENBURG [2]

[1] *Chevron Petroleum Technology Co., 1300 Beach Boulevard, La Habra, CA 90631-6374, U.S.A.*
[2] *University of British Columbia, Dept. of Geophysics and Astronomy, 129-2219 Main Mall, Vancouver, B.C., Canada V6T 1Z4.*

ABSTRACT

Aldridge, D.F. and Oldenburg, D.W., 1993. Two-dimensional tomographic inversion with finite-difference traveltimes. *Journal of Seismic Exploration*, 2: 257-274.

We present an iterative tomographic inversion procedure for reconstructing a two-dimensional velocity field from measured first arrival times. Two key features of this technique are (i) use of a finite-difference algorithm for rapid and accurate forward modeling of traveltimes, and (ii) incorporation of constraint information into the inversion in order to restrict the nonuniqueness inherent in large scale, nonlinear inverse problems.

Finite-difference traveltime computation provides a useful alternative to conventional raytracing in tomography. All first arrival wave types are handled with relative ease. Curved raypaths, needed for subsequent updating of the velocity model, are generated by following the steepest descent direction through a computed traveltime field from each receiver back to the source. The main limitation of the method is that it is restricted to first arrivals.

Constraint information may arise from known values of the subsurface velocity (e.g., from outcrops or well logs) or the imposition of reasonable geophysical characteristics, like smoothness, on the constructed velocity model. In either case, the data equations are augmented with additional linear constraint equations and a least squares solution of the entire system is obtained.

Analysis of a simulated double-well VSP plus crosswell experiment indicates that the inversion algorithm can accurately reconstruct a smoothly varying interwell velocity field. Inclusion of constraint information, in the form of horizontal and vertical first-difference regularization, allows the solution of a traveltime tomography problem that is otherwise severely underdetermined. Finally, the technique is successfully applied to two crosswell datasets acquired in a shallow oilfield in central California.

KEY WORDS: tomography, finite-difference traveltimes, constraints.

INTRODUCTION

Curved ray traveltime tomography was originally developed by Bois et al. (1972) for the purpose of estimating the seismic velocity distribution between two boreholes. Following their seminal work, several investigators advanced the technology of tomographic imaging with curved raypaths (Lytle and Dines, 1980; Bishop et al., 1985; McMechan et al., 1987; Bregman et al., 1989; White, 1989). Curved ray methods are necessary for accurately reconstructing the velocity field in highly refractive media. Although straight ray techniques are adequate in media with relatively small velocity variations, it is difficult to decide when this simplifying assumption of straight line raypaths becomes invalid. Hence, there is a compelling reason to use curved ray methods in all situations: they are based on a more accurate model of wave propagation through variable velocity media.

Traveltime tomography is a nonlinear inverse problem that can be solved by local linearization and iteration. Since the velocity field is updated on each cycle of the tomographic imaging procedure, rays have to be retraced between all source-receiver pairs. This raytracing constitutes a large part of the computational cost of curved ray tomographic inversion. Two-point raytracing between a specific source and receiver is an iterative process, and may encounter difficulties due to shadow zones and multipathing. In this study, we circumvent the problems associated with conventional raytracing by calculating traveltimes to all points of a two-dimensional slowness field with a rapid finite-difference algorithm (Vidale, 1988). Raypaths are then generated by following the steepest descent direction through the computed traveltimes from each receiver back to the source. This method yields the raypaths of all wave types that comprise first arrivals (body waves, head waves, and diffractions). Moreover, since arrival times are calculated throughout the slowness field, arbitrary recording geometries are easily accommodated.

In addition to rapid and accurate forward modeling, tomographic inversion requires the solution of a system of linear algebraic equations to obtain the improved velocity field. This solution may exhibit erratic and unphysical behavior due to noise in the traveltime data and/or ill-conditioning in the equations. Hence, some form of regularization is often used to stabilize the inversion. For example, Lytle and Dines (1980) introduce Laplacian smoothing into the system when calculating a perturbation to a slowness model. Bishop et al. (1985), Bregman et al. (1989), and White (1989) limit the size of the model perturbation by using the damped least squares method. Macrides et al. (1988) impose inequality constraints on a perturbation calculated via an algebraic reconstruction technique (ART) algorithm. Our approach is to apply linear equality constraints directly to the slowness model, rather than to a model perturbation, on each iteration of the inversion procedure. In addition to improving the mathematical conditioning of the system, the constraints allow the

introduction of *a priori* geological and geophysical knowledge about the model into the inversion. In particular, the constraints may arise from a desire to impose a preferred character, like flatness or smoothness, on the slowness solution. Alternately, we may seek a model that is close, in some quantitative sense, to a prescribed base model. Inclusion of these constraint equations restricts the nonuniqueness that is common in realistic tomographic inverse problems.

The nonlinear tomographic inversion procedure described in this paper consists of four basic steps:

1) calculation of first arrival traveltimes from each source location to all points of a gridded slowness field,
2) generation of raypaths between all source-receiver pairs,
3) solution of a large and sparse system of linear equations for a perturbation to the existing slowness model,
4) updating the slowness model.

This four-step process is initiated with an estimate of the true slowness function, and is repeated until an acceptable match is obtained between observed and calculated traveltimes. Subsequent sections describe these steps in more detail. The inversion procedure is demonstrated using synthetic traveltime data from simulated VSP and crosswell experiments. Finally, the technique is applied to a crosshole dataset acquired in a shallow oilfield in central California.

GENERAL THEORY AND MODEL REPRESENTATION

The traveltime of a seismic wave propagating through a slowness field $s(\mathbf{r})$ satisfies the eikonal equation

$$|\nabla t(\mathbf{r})|^2 = s(\mathbf{r})^2 \quad . \tag{1}$$

This is a nonlinear partial differential equation for the traveltime function $t(\mathbf{r})$. Linearization of the eikonal equation about a reference slowness model $s_0(\mathbf{r})$ yields an expression for the change in traveltime induced by a small slowness perturbation $\Delta s(\mathbf{r})$. The result is

$$\Delta t(\mathbf{r}) = \int_{L_0(\mathbf{r})} \Delta s \, dl_0 \quad , \tag{2}$$

where $L_0(\mathbf{r})$ is the raypath through the reference medium from the source to position $\mathbf{r}$. Hence, a small change in traveltime is linearly related to a small change in slowness.

We represent a two-dimensional slowness function s(x,z) by a set of K square cells, each with a uniform slowness value m_k (k = 1,2,...,K). Thus, within a cell, a raypath is a straight line segment. For a collection of raypaths between many source-receiver pairs, equation (2) is expressed as the matrix/vector product

$$\Delta t = A(m)\Delta m \quad , \tag{3}$$

where $A(m)$ is a matrix of raypath length segments within the square cells of the slowness model m. In the tomographic inversion problem, we seek a model perturbation Δm such that the improved model $m + \Delta m$ approximates the true slowness model associated with the measured traveltimes. Hence, the traveltime difference vector Δt is given by

$$\Delta t = t_{obs} - t_{prd}(m) \quad , \tag{4}$$

where t_{obs} is a vector of observed arrival times, and $t_{prd}(m)$ is a vector of predicted traveltimes computed from the known slowness model m. In principle, equation (3) can be solved for the required model perturbation. In practice, solution difficulties arise because the raypath matrix is usually nonsquare, large, sparse, and rank deficient. Moreover, since the observed traveltimes contain random errors, the system (3) may be inconsistent. In this case, an exact solution does not exist and a minimum misfit solution is usually sought. Finally, if the initial model m is a poor approximation to the true slowness, several iterations of the model updating procedure may be necessary before the magnitude of the traveltime residual vector Δt becomes acceptably small.

FORWARD MODELING

The first arrival times of a seismic wave propagating through a two-dimensional velocity structure are computed by Vidale's (1988) finite-difference scheme. This algorithm uses plane wavefront traveltime operators to extrapolate arrival times from point to point throughout a uniformly spaced grid. The method is rapid and accurate, and can be applied to a heterogeneous medium with moderate to strong velocity variations. Podvin and Lecomte (1991) and Aldridge and Oldenburg (1992) describe improvements to the local traveltime extrapolators that allow models with very strong velocity contrasts to be examined. The traveltimes of all wave types that comprise first arrivals (body waves, head waves, and diffractions) are calculated. Reflections and other later arrivals are not included; this represents a limitation of the technique as currently formulated.

Vidale's method is based on a centered finite-difference solution of the eikonal equation on each square cell of a gridded slowness field. Thus, the associated discretization error is second order in the grid cell size. An input slowness function $s(x,z)$ is sampled on a uniformly spaced two-dimensional grid. If the grid interval is h, then the sampled slowness values are given by $s_{ij} = s(x_i, z_j)$, where $x_i = x_{min} + (i-1)h$ and $z_j = z_{min} + (j-1)h$ (with $i=1,2,..., I$ and $j=1,2,..., J$). Since there are I J grid points, there are $K = (I-1)(J-1)$ square cells. The slowness assigned to a particular cell is the arithmetic mean of the slowness values at the four bounding grid points:

$$m_k = \tfrac{1}{4}(s_{ij} + s_{i+1,j} + s_{i,j+1} + s_{i+1,j+1}) \quad , \tag{5}$$

where $k = i + (I-1)(j-1)$. With this indexing scheme, the elements of the vector **m** constitute a row-ordered sequence of the two-dimensional array of cell slowness values. An individual cell is referenced either by the coordinate indices of its upper left corner (ij) or by its sequential index (k).

Calculations are initiated at a designated source point (x_s, z_s) (not necessarily coincident with a grid node) within the slowness model. Since wavefronts are strongly curved in the immediate vicinity of a point source, plane wavefront traveltime extrapolators are inappropriate in this region. Furthermore, near-source inaccuracies will be propagated to all greater distances. In order to mitigate these effects, we calculate arrival times in a near-source rectangle via the exact traveltime formula for a linear velocity field. The coefficients defining the linear velocity function are obtained by performing a least squares fit to the velocity samples $v_{ij} = 1/s_{ij}$ surrounding the source.

The finite-difference algorithm calculates a traveltime t_{ij} at every grid point of the slowness field. If a receiver is not located on a grid node, then an interpolator is needed to estimate the arrival time at the actual receiver position. Simple bilinear interpolation provides adequate accuracy. Hence, if a receiver with coordinates (x_r, z_r) is located within cell ij, then define the dimensionless quantities $p = (x_r - x_i)/h$ and $q = (z_r - z_j)/h$. The interpolated traveltime is given by

$$t(x_r, z_r) = (1-p)(1-q)t_{ij} + p(1-q)t_{i+1,j} + q(1-p)t_{i,j+1} + pqt_{i+1,j+1} \quad . \tag{6}$$

If the four arrival times bounding cell ij are due to local plane wave propagation, then equation (6) is an exact expression for the traveltime at the interior point (x_r, z_r). In other cases, the interpolator (6) has accuracy $O(h^2)$ (Dahlquist and Björk, 1974, p. 319) and thus is consistent with the level of accuracy associated with the forward modeling scheme.

RAY GENERATION

Raypaths are generated by following the steepest descent direction through a computed traveltime field from each receiver back to the corresponding source point. This strategy was originally suggested by Vidale (1988) and has recently been implemented (in a form somewhat different from that described here) by Podvin and Lecomte (1991).

The horizontal and vertical components of the traveltime gradient vector within cell i j are approximated by the centered finite-difference formulae

$$\partial t/\partial x \simeq [(t_{i+1,\,j} + t_{i+1,\,j+1}) - (t_{i\,j} + t_{i,\,j+1})]/2h \quad , \tag{7}$$

$$\partial t/\partial z \simeq [(t_{i,\,j+1} + t_{i+1,\,j+1}) - (t_{i\,j} + t_{i+1,\,j})]/2h \quad . \tag{8}$$

The assignment of a constant traveltime gradient to a cell is compatible with the assumption of locally plane wavefronts used in the forward modeling algorithm. The steepest descent direction is opposite to the gradient direction of the traveltime field. Hence, within cell i j (or k) the steepest descent direction is defined by the angle

$$\theta_k = \tan^{-1}[(\partial t/\partial z)/(\partial t/\partial x)] + \pi \quad . \tag{9}$$

θ_k is measured clockwise from the positive horizontal axis. For a fixed source, all raypaths that cross cell i j have this same orientation angle. The lengths of the raypath segments within the cell range from zero to a maximum of $\sqrt{2}h$.

A representative situation for cell i j is depicted in Fig. 1. The raypath enters the cell at point A on its right boundary with coordinates (x_a, z_a). Depending on the value of the steepest descent angle assigned to the cell, the ray may exit on any of the remaining three sides or one of the four corners. The logic that selects one of these possibilities is given in the first column of Table 1, where α_1 and α_2 are positive acute angles defined by

$$\alpha_1 = \tan^{-1}[(z_{j+1} - z_a)/h] \,, \quad \alpha_2 = \tan^{-1}[(z_a - z_j)/h] \quad .$$

These two angles are illustrated in Fig. 1. After an exit option is selected, the coordinates of the exit point B are easily determined (columns 2 and 3 in Table 1). These coordinates (x_b, z_b) constitute the entry point coordinates for the next cell that the ray crosses (columns 4 and 5 in Table 1). In the particular case displayed, the raypath enters cell i, j+1 on its top boundary. Hence, a *different* logical scheme is required to extend the raypath across this next cell. A total of eight logical tables are necessary to handle all of the possibilities. These correspond to a raypath entering a cell on any of its four sides or four corners.
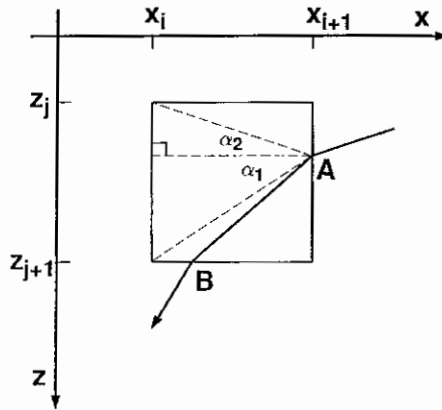
Fig. 1. Raypath (heavy line) traced through square cell i j of a 2-D slowness model. Ray enters cell at point A, follows the local steepest descent direction across the cell, and exits at point B.

Ray tracing is initiated at each receiver position and continues until the raypath arrives at the boundary of a prescribed near-source zone. The final portion of the raypath is then taken to be a straight line segment from the boundary point directly to the source position (x_s, z_s). This ray termination procedure is designed to overcome difficulties associated with nonuniformity of the traveltime gradient vector in close proximity to the source.

Table 1. Ray tracing logic for an entry point on the right side of a square grid cell. Column 1 gives possible ranges for the steepest descent angle θ_k assigned to the cell. Angles α_1 and α_2 are defined in the text and illustrated in Fig. 1. Columns 2 and 3 give the horizontal and vertical coordinates of the ray exit point, respectively. (x_a, z_a) are the ray entry point coordinates. Columns 4 and 5 give the indices of the next cell that the ray enters.

ANGLE RANGE	EXIT COORDINATES		NEXT CELL	
$0 < \theta_k \leq \pi/2$	x_{i+1}	z_{j+1}	$i+1$	$j+1$
$\pi/2 < \theta_k < \pi - \alpha_1$	$x_a + (z_{j+1} - z_a)\cot\theta_k$	z_{j+1}	i	$j+1$
$\theta_k = \pi - \alpha_1$	x_i	z_{j+1}	$i-1$	$j+1$
$\pi - \alpha_1 < \theta_k < \pi + \alpha_2$	x_i	$z_a - h\tan\theta_k$	$i-1$	j
$\theta_k = \pi + \alpha_2$	x_i	z_j	$i-1$	$j-1$
$\pi + \alpha_2 < \theta_k < 3\pi/2$	$x_a + (z_j - z_a)\cot\theta_k$	z_j	i	$j-1$
$3\pi/2 \leq \theta_k < 2\pi$	x_{i+1}	z_j	$i+1$	$j-1$

Fig. 2a is a contour plot of a velocity model bounded by two vertical boreholes. A shallow low velocity anomaly overlies a dipping, higher velocity zone. The first arrival wavefronts from a surface source located between the boreholes are illustrated in Fig. 2b. The wavefronts are retarded by the low velocity zone and advance more rapidly through the high velocity zone. In addition, Fig. 2b displays the raypaths traced through this time field from 18 downhole receivers back to the source. The raypaths are orthogonal to the wavefronts, as expected.
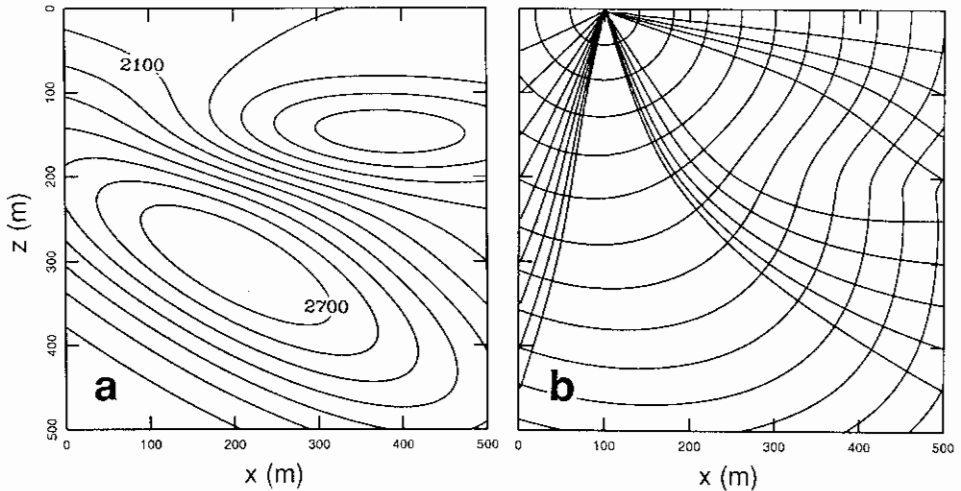
Fig. 2. (a) Velocity model (contour interval = 100 m/s) with a horizontal low velocity zone and a dipping high velocity zone. Maximum velocity = 2800 m/s; minimum velocity = 1633 m/s. (b) Wavefronts (contour interval = 20 ms) and raypaths generated by a surface source. The raypaths are traced from 18 downhole receivers back to the surface source.

INVERSION MATHEMATICS

As indicated previously, system (3) is typically ill-conditioned and inconsistent. Hence, an undamped least squares solution (i.e., a solution of $A^TA\Delta m = A^T\Delta t$) may yield a model update vector with relatively large and unrealistic cell-to-cell variations in slowness. Robust inversion algorithms handle the inconsistency of the equations, and the nonuniqueness arising from ill-conditioning, by minimizing an objective function that is the sum of a misfit term Φ_d and a model dependent term Φ_m. A commonly used misfit measure employs the L_2 norm: $\Phi_d = \| W_d(A\Delta m - \Delta t) \|^2$ where W_d is a prescribed data weighting matrix. This matrix is usually diagonal with elements inversely proportional to estimated standard errors for each datum. For simplicity, we assume that the data are uniformly weighted; W_d then reduces to the identity matrix.

The model objective function term Φ_m may take various forms, but a typical objective function for this two-dimensional problem is

$$\Phi_m = \mu_1^2 \int\int w_1(x,z)(s-s_{base})^2 dxdz + \mu_2^2 \int\int w_2(x,z)[\partial(s-s_{base})/\partial x]^2 dxdz$$

$$+ \mu_3^2 \int\int w_3(x,z)[\partial(s-s_{base})/\partial z]^2 dxdz \quad . \qquad (10)$$

The weighting functions w_1, w_2, and w_3 are specified by the user. These functions can be tailored so that the constructed slowness model $s(x,z)$ is preferentially close to a known base model $s_{base}(x,z)$ at certain locations (for instance, near the boreholes), or so that penalties against horizontal and vertical variation can be imposed in certain regions. The scalars μ_1, μ_2, and μ_3 control the relative importance of the various terms.

The discrete form of (10), after explicitly writing the updated model as $m + \Delta m$, is

$$\Phi_m = \sum_{n=1}^{3} \mu_n^2 \| B_n(m + \Delta m - m_{base}) \|^2 \quad , \qquad (11)$$

where the matrices B_n represent the operators in the integrands of (10). Hence, the total objective function is

$$\Phi(\Delta m) = \| A\Delta m - \Delta t \|^2 + \sum_{n=1}^{N} \mu_n^2 \| B_n(m + \Delta m - m_{base}) \|^2 \quad , \qquad (12)$$

where, for generality, a total of N distinct terms is now allowed in the sum. Extremizing Φ with respect to Δm yields the linear algebraic equations

$$[A^T A + \sum_{n=1}^{N} \mu_n^2 B_n^T B_n]\Delta m = A^T \Delta t + \sum_{n=1}^{N} \mu_n^2 B_n^T B_n(m_{base} - m) \quad . \qquad (13)$$

For nonzero μ_n^2, the coefficient matrix in this equation is usually nonsingular. The required model perturbation Δm can be obtained by solving (13) using standard techniques of numerical linear algebra. However, the coefficient matrix is large (K × K, where K is the number of slowness cells) and may be dense even if the original raypath and constraint matrices are sparse. Hence, it is advantageous to seek a solution method that avoids explicitly forming the square matrices $A^T A$ and $B_n^T B_n$.

It is straightforward to demonstrate that (13) are the normal equations associated with the least squares solution of the rectangular system

$$
\begin{bmatrix} \mathbf{A} \\ \mu_1\mathbf{B}_1 \\ \vdots \\ \mu_N\mathbf{B}_N \end{bmatrix} \Delta\mathbf{m} = \begin{bmatrix} \Delta\mathbf{t} \\ \mu_1\mathbf{B}_1(\mathbf{m}_{base} - \mathbf{m}) \\ \vdots \\ \mu_N\mathbf{B}_N(\mathbf{m}_{base} - \mathbf{m}) \end{bmatrix} \quad . \tag{14}
$$

When written in this manner, it is clear that the various terms in the model objective function (10) can be interpreted as linear equality constraints on the updated model of the form

$$
\mathbf{B}_n(\mathbf{m} + \Delta\mathbf{m}) = \mathbf{B}_n\mathbf{m}_{base} \quad . \tag{15}
$$

We use algorithm LSQR (Paige and Saunders, 1982) to solve equation (14) directly for $\Delta\mathbf{m}$. LSQR is an iterative solution technique for large and sparse systems of linear equations that is closely related to the conjugate gradient method. It is designed to seek the minimum norm least squares solution of a set of equations. Numerical studies of LSQR applied to the tomographic inversion problem indicate that it is both rapid and accurate (Nolet, 1985; Scales, 1987). A simple FORTRAN version of the LSQR algorithm is given by Nolet (1987).

The dimensions of the coefficient matrix in (14) are $(N_{data} + N_{cons}) \times K$, where N_{data} and N_{cons} are the number of data and constraint equations, respectively. Since this matrix may be large and sparse, a significant reduction in storage space is achieved by storing only the nonzero elements in a one dimensional array. We use the full index scheme described by Scales (1987) to store and address the matrix elements. With this storage method, the sparse matrix/vector multiplications required by the LSQR algorithm are particularly simple to implement.

Finally, the correction to the slowness value at grid point i j is determined by averaging the slowness perturbations calculated for the four surrounding cells:

$$
\Delta s_{ij} = \tfrac{1}{4}(\Delta m_{k-I} + \Delta m_{k-I+1} + \Delta m_{k-1} + \Delta m_k) \quad , \tag{16}
$$

where $k = i + (I-1)(j-1)$. Grid points located on the edges (corners) of the slowness model are updated by adding the average of the perturbations associated with neighboring two (one) cells. After all grid points are updated, forward modeling of traveltimes for the next iteration of the inversion can proceed.

MODEL CONSTRAINT EQUATIONS

There is considerable latitude is designing the model objective function term Φ_m and correspondingly, the individual matrices $\mathbf{B}_n$ used in the constraint

equations. In our examples, the weighting functions w_1, w_2 and w_3 in equation (10) are taken to be unity. Then, the constraint matrices are easily generated from a two-dimensional 'operator' or 'filter' with five specified constants c_1, c_2, c_3, c_4 and c_5. Fig. 3 depicts the application of this operator to interior cell i j of a slowness model. Using the row-ordered indexing scheme, the kth component of the filtered image **Bm** is given by

$$c_1 m_{k+1} + c_2 m_{k+I-1} + c_3 m_{k-1} + c_4 m_{k-I+1} + c_5 m_k \quad .$$

Edge cells are handled by conceptually extending the slowness model beyond the defined region with the local cell slowness values. For example, application of the 5-cell operator to the upper left corner cell (i = 1, j = 1 corresponding to k = 1) of the model **m** is via the formula

$$c_1 m_2 + c_2 m_I + (c_3 + c_4 + c_5) m_1 \quad .$$

One such constraint is applied to each cell of the slowness model. Development of the matrix representation **B** for this set of equations is a matter of proper row and column indexing.

The 5-cell operator is an extremely simple and flexible mechanism for introducing various types of model roughness penalties into tomographic inversion. Some common examples include:

Case 1: $c_5 = 1$ and all other $c_i = 0$. An individual cell slowness is not constrained by its immediate neighbors. Rather, inversion produces a model that is closest, in the least squares sense, to a given target model m_{base}. This emulates the first term of Φ_m in equation (10).
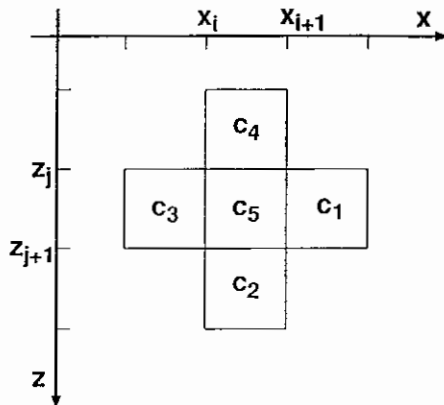

Fig. 3. Schematic representation of the 5-cell constraint operator applied to cell i j of a slowness model. The slowness values in five neighboring cells are multiplied by constants c_1 through c_5 and the products are summed.

Case 2: $c_1 = 1/2h$, $c_3 = -1/2h$ and all other $c_i = 0$. This operator is a centered finite-difference approximation to the horizontal derivative of the slowness field. A similar approximation to the vertical derivative is obtained by setting $c_2 = 1/2h$, $c_4 = -1/2h$ and all other $c_i = 0$. These operators introduce first-difference regularization, or flattening, into the procedure. Inversion produces a model with first derivatives that are close, in the L_2 norm sense, to those of the prescribed base model $\mathbf{m}_{base}$. These operators emulate the second and third terms of Φ_m in equation (10).

Case 3: $c_1 = 1/h^2$, $c_5 = -2/h^2$, $c_3 = 1/h^2$ and all other $c_i = 0$. This operator, as well as its vertical counterpart, introduces second-difference regularization, or smoothing, into the inversion.

Case 4: $c_1 = c_2 = c_3 = c_4 = 1/h^2$ and $c_5 = -4/h^2$. This operator incorporates Laplacian smoothing into the inversion.

Combinations of these cases are easily implemented (this is the reason for generalizing to N terms in the sum of expression (12)). In the following synthetic and field data examples, we apply the flattening constraints described in *Case 2* above.
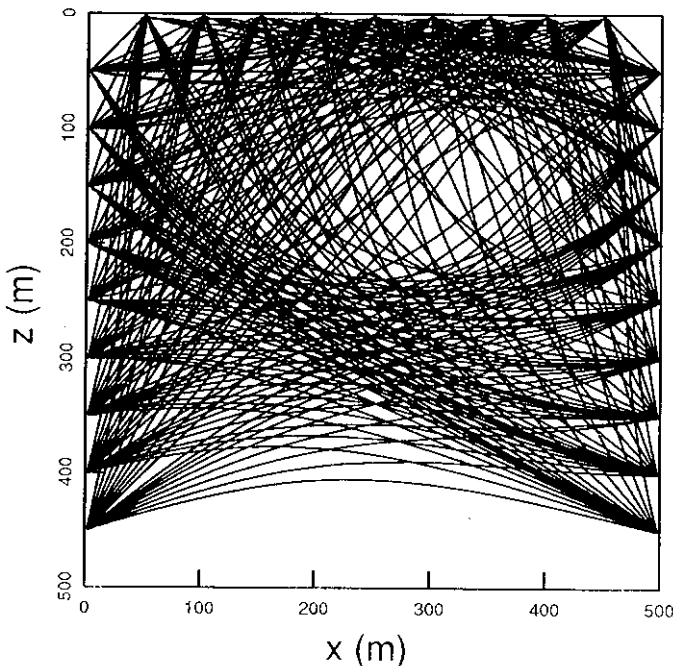

Fig. 4. 243 raypaths traced through the velocity field of Fig. 2a. These rays link all source–receiver pairs of a combined double-well VSP and crosswell experiment.

SYNTHETIC EXAMPLES

The examples presented in this section demonstrate the ability of the tomographic inversion procedure to image a smoothly varying velocity field. Fig. 2a displays the 500 m × 500 m velocity model used to generate synthetic traveltime data. Since the grid interval is h = 5 m, there are I J = 10201 grid points used for the forward modeling and K = 10,000 square cells used in the inversion.

The data acquisition geometry used for the first example simulates a double-well VSP plus crosswell experiment. Nine surface sources, located between two vertical boreholes, are spaced 50 m apart. Traveltimes are recorded by 18 borehole receivers (9 per well; 50 m separation) from each source position. In addition, the 9 downhole receivers in the right well record traveltimes from 9 sources symmetrically placed in the left well. The complete set of 243 raypaths linking all source-receiver pairs is illustrated in Fig. 4. Note that these first arrival raypaths tend to avoid the low velocity zone, resulting in a region of reduced ray coverage. Furthermore, no raypaths penetrate below 450 m depth.

Contoured velocity tomograms obtained by inverting the combined VSP and crosswell traveltimes are displayed in Fig. 5. Both horizontal and vertical first-difference constraints are imposed in the iterative inversions. Initial and base slowness models are uniform, and are obtained from the slowness value that minimizes the rms traveltime residual. In Fig. 5a, numerically exact traveltimes are inverted. In eleven iterations, the initial rms traveltime misfit of 18.2 ms is reduced to ~ 0.5 ms, which is about 0.25 % of the rms value of the synthetic data.
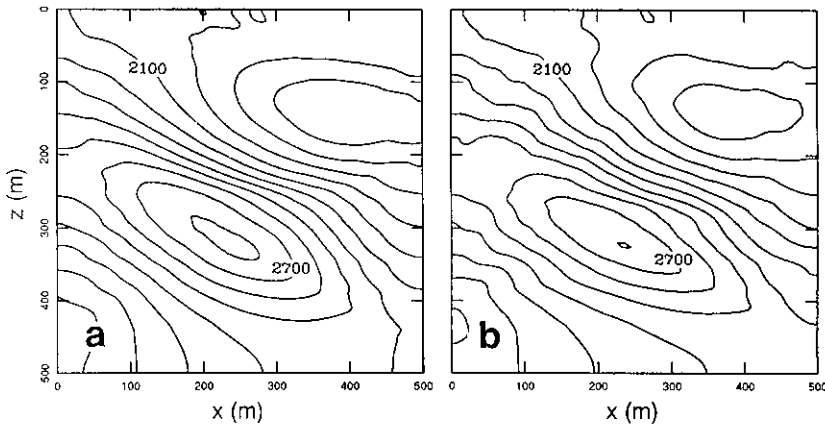

Fig. 5. Reconstructed velocity models (contour interval = 100 m/s) obtained by inverting combined VSP and crosswell traveltimes. (a) Exact traveltimes. Max velocity = 2822 m/s; min velocity = 1730 m/s. (b) Noisy traveltimes. Max velocity = 2803 m/s; min velocity = 1745 m/s.

Fig. 5b illustrates that the inversion method is stable when the synthetic traveltimes are contaminated with small amounts of random noise. Random numbers drawn from a uniform probability distribution on $\pm$ 4 ms are added to the exact times. The convergence criterion for terminating iterations is arbitrarily selected to be 2.5 ms of rms traveltime misfit (approximately one standard deviation of the noise). An accurate velocity reconstruction results when the weights of the flattening constraints (μ_2 and μ_3 in equation (14)) are set sufficiently high.

The main features of the true velocity model are recovered by both of the inversions depicted in Fig. 5. The location and amplitude of the dipping high velocity anomaly are approximately correct. Also, the shallow low velocity zone has been detected and correctly positioned, although the computed velocity value at its center is about 90 m/s too high. This effect is associated with the reduced raypath density in this area of the model. The principal difference between the two reconstructions appears in the region below 400 m depth, where raypath coverage is negligible.
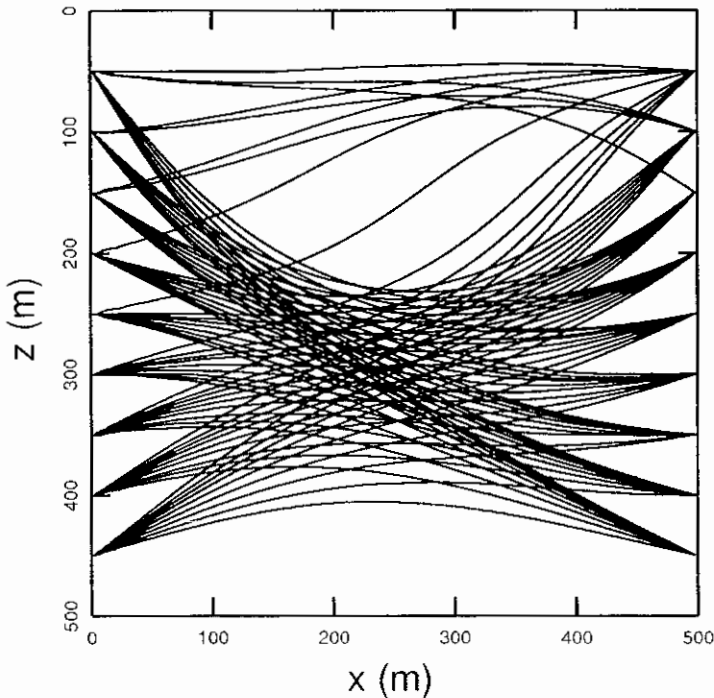

Fig. 6. 81 crosswell raypaths traced through the velocity model of Fig. 2a. 9 sources are in left well and 9 receivers are in right well.

The next example examines the ability of the constrained inversion algorithm to recover the interwell velocity field when only crosshole traveltimes are available. Fig. 6 displays the 81 crosswell raypaths. The zone of reduced ray coverage at shallow depths is much more extensive. Images obtained by inverting error free traveltimes are illustrated in Fig. 7. Once again, both horizontal and vertical flattening constraints are applied. In Fig. 7a, the initial and base slowness models are uniform and equal to each other. The computed image displays a shallow low velocity zone and a deeper, dipping high velocity zone. However, the peak of the high velocity anomaly is shifted downdip by a significant amount. The result in Fig. 7b is obtained from nonuniform initial and base slowness models constructed by horizontally interpolating the borehole slowness values. Additionally, the slownesses of the cells adjacent to the two boreholes are constrained to be equal to the true values. In an actual field experiment, this information may be available from borehole velocity logs. There is some improvement in the velocity reconstruction compared with Fig. 7a. In particular, the high velocity zone at depth has moved updip towards its true location. The rms traveltime misfits associated with both tomograms in Fig. 7 are ~ 0.6 ms. This example illustrates the well known ambiguity inherent in tomographic inversion when only crosshole traveltimes are used.
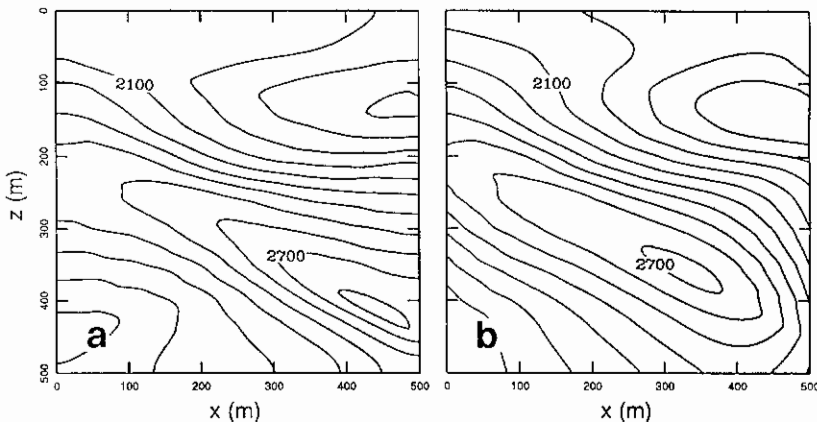

Fig. 7. Reconstructed velocity models (contour interval = 100 m/s) obtained by inverting only the crosswell traveltimes. (a) Uniform initial and base models; no borehole velocity constraints. Max velocity = 2825 m/s; min velocity = 1790 m/s. (b) Nonuniform initial and base models; borehole velocity constraints applied. Max velocity = 2722 m/s; min velocity = 1709 m/s.

FIELD DATA EXAMPLE

Our final example applies the tomographic inversion procedure to two crosswell traveltime datasets recently recorded in the Midway-Sunset oilfield in central California. The reservoir rocks of the Midway-Sunset field have undergone years of steam drive in an effort to enhance oil production. In

1989-90, foam was injected into the reservoir in an attempt to control steam mobility. The changing conditions in the reservoir were monitored by crosswell surveys conducted in July 1989 and August 1990. Paulsson et al. (1992) provide a detailed description of these experiments, and give pertinent aspects of the geological and geophysical environments. Moreover, their tomograms (calculated via an ART algorithm) provide a basis for comparison with the results presented here.

Fig. 8 displays P-wave velocity tomograms between well pair 68J-68Z in the Midway-Sunset oilfield. The image in Fig. 8a is computed from crosswell traveltimes acquired in July 1989, shortly after the onset of foam injection. The velocity field in Fig. 8b is obtained by inverting traveltimes recorded 13 months later in August 1990. The number of observed first arrival times used for the two inversions differ due to varying recording geometries and noise conditions.
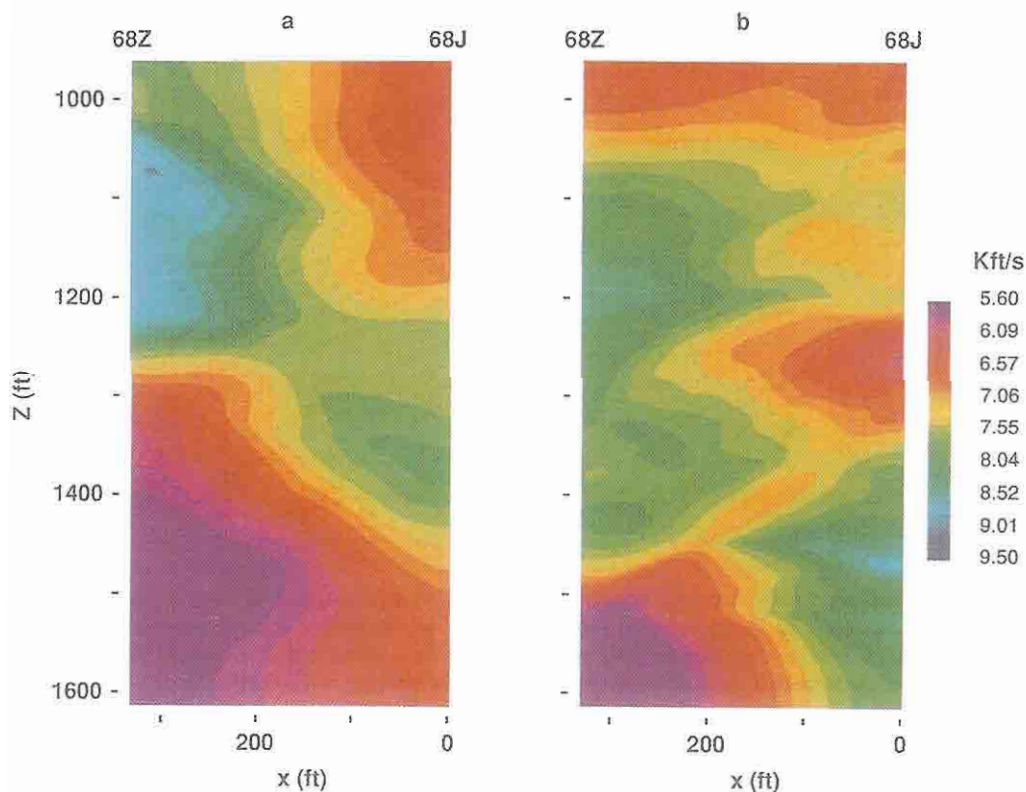

Fig. 8. P-wave velocity tomograms between well pair 68J-68Z in the Midway-Sunset oilfield. (a) July 1989 survey. (b) August 1990 survey.

There are 436 raypaths used for Fig. 8a, and 933 raypaths used in Fig. 8b. Each tomogram consists of 8320 square pixels, 5 ft on a side. Also, the color scale is identical to that used by Paulsson et al. (1992, Figs. 6 and 7) in order to facilitate comparison with their results.

The iterative inversions are initiated with uniform slowness models calculated by the same method used for the synthetic examples. Both horizontal and vertical flattening constraints are imposed, and base slowness models are identical to the initial models. In order to determine appropriate numerical values for the tradeoff parameters in equation (14), repeated inversion runs are executed. The largest values of μ_2 and μ_3 that yield a final rms traveltime misfit of ~ 1 ms are retained. In this manner, the inversions reconstruct the flattest (i.e., minimum first derivative norm) models for the specified misfit level. Smaller values of these weights yield slowness models that overfit the error contaminated traveltimes, and may produce spurious structures that are merely artifacts of the noise.

The tomograms of Fig. 8 are similar to equivalent tomograms displayed in Figs. 6 and 7 of Paulsson et al. (1992). Evidently, the velocity structure underwent substantial alteration in the 13 months intervening between the two crosswell surveys. A detailed interpretation of these changes is discussed at length by Paulsson et al. (1992).

CONCLUSION

Finite-difference traveltime computation offers an attractive alternative to conventional raytracing for tomographic inversion purposes. The method is sufficiently rapid and accurate, and handles all of the various wave types that constitute first arrivals (body waves, head waves, and diffractions). Moreover, since traveltimes are computed throughout a slowness model, very general recording geometries are easily accommodated. The main limitation of the technique is that it is restricted to first arriving waves. Hence, the present formulation cannot be applied to the reflection tomography problem. However, current efforts to generalize finite-difference computation methods to reflection traveltimes (e.g., Podvin and Lecomte, 1991) are encouraging. The introduction of constraint information into traveltime tomography is a responsible way to address the nonuniqueness inherent in this nonlinear inverse problem. Constraining information may arise from known geological or geophysical properties of the subsurface velocity model (i.e., from outcrops or borehole logs). Alternately, constraints may derive from a desire to impose certain reasonable attributes, like flatness or smoothness, on the constructed model. Our method of incorporating constraints into the mathematical inversion procedure is adaptable to either viewpoint. Linear equality constraints are applied directly to the constructed model, rather than to a model perturbation, and are satisfied

in the least squares sense. Our examples illustrate the imposition of flattening constraints, prescribed base models, and borehole velocities in the reconstruction of a smoothly varying interwell velocity field. Inclusion of this information allows the solution of an inverse problem that is otherwise strongly underdetermined.

ACKNOWLEDGEMENTS

REFERENCES

Aldridge, D.F. and Oldenburg, D.W., 1992. Refractor imaging using an automated wavefront reconstruction method. Geophysics, 57: 378-385.

Bishop, T.N., Bube, K.P., Cutler, R.T., Langan, R.T., Love, P.L., Resnick, J.R., Shuey, R.T., Spindler, D.A. and Wyld, H.W., 1985. Tomographic determination of velocity and depth in laterally varying media. Geophysics, 50: 903-923.

Bois, P., La Porte, M., Lavergne, M. and Thomas, G., 1972. Well-to-well seismic measurements. Geophysics, 37: 471-480.

Bregman, N.D., Bailey, R.C. and Chapman, C.H., 1989. Crosshole seismic tomography. Geophysics, 54: 200-215.

Dahlquist, G. and Björck, A., 1974. Numerical Methods. Prentice-Hall, Inc.

Lytle, R.J. and Dines, K.A., 1980. Iterative ray tracing between boreholes for underground image reconstruction. IEEE Trans. Geosci. Remote Sensing, 18: 234-240.

Macrides, C.G., Kanasewich, E.R. and Bharatha, S., 1988. Multiborehole seismic imaging in steam injection heavy oil recovery projects. Geophysics, 53: 65-75.

McMechan, G.A., Harris, J.M. and Anderson, L.M., 1987. Cross-hole tomography for strongly variable media with applications to scale model data. BSSA, 77: 1945-1960.

Nolet, G., 1985. Solving or resolving inadequate and noisy tomographic systems. J. Comp. Phys., 61: 463-482.

Nolet, G., 1987. Seismic wave propagation and seismic tomography. In: Nolet, G. (Ed.), Seismic Tomography. D. Reidel Publ. Co., Dordrecht. pp. 1-23.

Paige, C.C. and Saunders, M.A., 1982. LSQR: an algorithm for sparse linear equations and sparse least squares. ACM Trans. Math. Software, 8: 43-71.

Paulsson, B.N.P., Smith, M.E., Tucker, K.E. and Fairborn, J.W., 1992. Characterization of a steamed oil reservoir using cross-well seismology. The Leading Edge, 11, no. 7: 24-32.

Podvin, P. and Lecomte, I., 1991. Finite difference computation of traveltimes in very contrasted velocity models: a massively parallel approach and its associated tools. Geophys. J. Int., 105: 271-284.

Scales, J.A., 1987. Tomographic inversion via the conjugate gradient method. Geophysics, 52: 179-185.

Vidale, J., 1988. Finite-difference calculation of travel times. BSSA, 78: 2062-2076.

White, D.J., 1989. Two-dimensional seismic refraction tomography. Geophys. J., 97: 223-245.